

Mie-type GaAs nanopillar array resonators for negative electron affinity photocathodes

XINCUN PENG,^{1,2,3}  MATT POELKER,² MARCY STUTZMAN,² BIN TANG,¹ SHUKUI ZHANG,^{2,4} AND JIJUN ZOU^{1,2,5}

¹Engineering Research Center of New Energy Technology of Jiangxi Province, East China University of Technology, Nanchang 330013, China

²Thomas Jefferson National Accelerator Facility, 12000 Jefferson Avenue, Newport News, Virginia 23606, USA

³xcpeng@ecit.cn

⁴shukui@jlab.org

⁵jjzou@ecit.cn

Abstract: This paper presents modeling results of Mie-type GaAs nanopillar array resonant structures and the design of negative electron affinity photocathodes based on Spicer's three-step model. For direct-bandgap GaAs with high intrinsic absorption coefficient in the 500 ~ 850 nm spectral range, photoelectrons were found to be highly localized inside the nanopillars near the top and side surfaces where electrons can be efficiently transported and emitted into vacuum, and the light reflectance can be reduced to ~1% level at resonance wavelengths. Predictions of spectrally resolved photoemission indicate that these nanophotonics resonators, when properly optimized, can increase the photo-electron emission quantum efficiency at resonance wavelengths to levels limited only by the surface-electron escape probability, significantly outperforming traditional flat wafer photocathodes. Ultrafast photoelectric response is also expected from these nanostructured photocathodes due to the much shorter photoelectron transport distance in nanopillars compared to flat wafers. Given these unique optoelectronic properties, GaAs nanophotonic resonance structured photocathodes represent a very promising alternative to photocathodes with flat surfaces that are widely used in many applications today.

© 2020 Optical Society of America under the terms of the [OSA Open Access Publishing Agreement](#)

1. Introduction

Negative electron affinity (NEA) photocathodes, in which the photo-excited electrons are transported to the surface and emitted to vacuum, have been successfully used in areas such as outer space-based detection [1], high-resolution low-light-level spectral imaging [2–6], large-scale electron accelerators [7–11], low-energy electron microscopes [12–13], and electron beam lithography [14]. However, there has been an ever increasing demand for robust photocathodes with high quantum efficiency (*QE*), faster photoelectric response, longer operating lifetime, wider spectral response range and higher spin polarization [15–16], in particular when it comes to applications requiring high average current and/or high bunch charge typical of some large scale electron accelerators and accelerator-based light sources. Photo-electron emission from flat film-type structures, such as graded doping/band-gap layers [17–18] and distributed Bragg reflectors [19], have been explored to increase the *QE* of the gallium arsenide (GaAs) based photocathodes. However, the *QE* of the flat film-type device is always limited by the mismatch between the minority-carrier diffusion length and the optical absorption depth. In addition, a large portion of the incident light (>35%) is reflected from the surface of the flat film-like surface due to the high index of refraction of GaAs, which not only decreases *QE* but also generates unintended and unwanted photoemission in electron guns [15].

High-index of refraction semiconductors with sub-wavelength nanostructures have attracted increased attention due to their ability to support Mie-type geometrical resonances, and for

their compatibility with standard semiconductor device fabrication techniques [20–22]. In the visible and near infrared spectral range, Si nanoparticles have been considered ideal Mie-type resonators and have attracted significant interests [23–26]. However, little attention has been paid to GaAs resonators and so far, no results have been reported relevant to photocathode applications. Compared with indirect-bandgap Si, the direct-bandgap GaAs has a much larger light absorption coefficient, which leads to strong light absorption in resonators. In the visible waveband, every photon absorbed by GaAs can excite an electron-hole pair and contribute to the QE of optoelectronic devices.

To exploit Mie-type resonance for a photocathode application, the light must be efficiently absorbed and concentrated within the fabricated nano-structure [27–28]. Due to the much smaller size of the nano-resonators compared with traditional film structures, the process of light absorption can be efficiently decoupled from that of carrier collection, and improved optoelectronic efficiency has been reported in GaAs nano-resonator devices [29–33]. For typical diode-type devices such as solar cells, photodetectors, etc., the p-n junctions and electrodes serve indispensable functions, and it is difficult to realize these complex device functions inside the nano-scale resonators [30,33]. However, because the only functional part of the NEA photocathode is the p -type GaAs [34], it is much simpler to fabricate nano-scale photocathodes compared to diodes. These features make GaAs an excellent candidate for designing NEA photocathodes with nanostructured resonator surfaces.

In this work, a new type of nano-structured NEA photocathode is presented, in which the p -type GaAs Nanopillar-array (NPA) Mie-type resonator serves to enhance the photoelectron emission of the photocathode. The photoelectron emission processes of the NPA photocathodes were analyzed based on Spicer's three-step model [35–36], which consists of photoelectron generation, electron transport to the surface, and escape across the surface into vacuum. The photoelectron generation and transport efficiencies were modeled using Lumerical Finite Difference Time Domain (FDTD) [37] and Cogenda Technology Computer-Aided Design (TCAD) [38] tools, respectively. The surface-electron escape probability was obtained by fitting the theoretical model to measured QE of typical GaAs photocathodes [36]. Based on these methods, we show excellent light management performance of the nanophotonic resonators, which provides exceptionally low surface reflectance and significant QE enhancement across the entire 500 ~ 850 nm waveband. Furthermore, the photoelectric response time for NPA photocathodes is expected to be ultrafast due to the much shorter photoelectron transport distance in the nanopillars compared to flat wafers. We conclude that GaAs NPA resonant structures can be designed and optimized to significantly improve photoemission performance of NEA photocathodes, which could benefit applications such as high-resolution night-vision imaging and large-scale electron accelerators.

2. Device structure and theoretical model

Figure 1(a) shows one unit-cell of the GaAs NPA. Unit cells would be repeated many times, with nano-pillars set at equal-distance and arranged on a p -type GaAs substrate. The chemicals cesium and fluorine cover the entire surface – pillars and substrate – and are used to activate the surface to the NEA state [34]. The relevant parameters that describe the geometry of the NPA are the period of the square lattice P , pillar diameter D , and pillar height H . By placing periodic boundary conditions, simulations were carried out within one unit-cell to model the properties of the periodic nanopillars on a square lattice.

Spicer's three-step model [35–36], illustrated in Fig. 1(b), was used to assess photocathode performance. The first step is photoexcitation (process A in Fig. 1(b)), described as the probability of absorbing an incident photon which in turn generates an electron-hole pair (P_g). This process was modeled through FDTD calculations of the interaction between light and GaAs [37]. Figure 1(c) shows the cross-section of the FDTD setup. Virtual two-dimensional light power meters in the x-y plane are positioned on top and bottom of the NPA for monitoring reflection

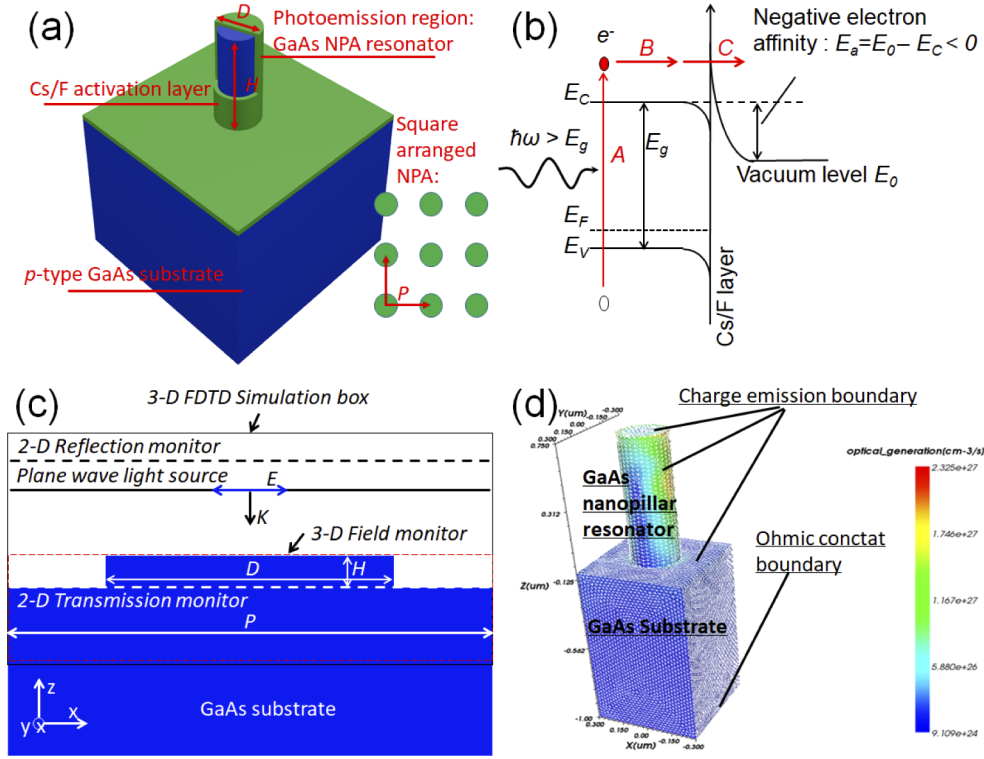


Fig. 1. Device structure and theoretical model of GaAs NPA photocathode. (a) Depiction of one unit cell of the GaAs NPA photocathode. (b) Photoelectron emission processes and electronic band structure of NEA photocathode based on Spicer's model. (c) Cross-section of the FDTD setup for simulating the optical properties of GaAs NPA. (d) TCAD setup for analyzing the photoemission properties of GaAs NPA photocathode.

and transmission, respectively. A cuboid three-dimensional field monitor is positioned around the nanopillar to monitor the spatial distribution of the electric field intensity ($E(\lambda, x, y, z)$) for the incident plane wave light with wavelength λ . The generation rate of the electron-hole pairs ($g(\lambda, x, y, z)$) in $\text{pairs} \cdot \text{cm}^{-3} \cdot \text{s}^{-1}$ can be calculated as

$$g(\lambda, x, y, z) = \frac{\pi \epsilon'' E(\lambda, x, y, z)^2}{h} \quad (1)$$

where h and ϵ'' are Planck's constant and the imaginary part of the GaAs permittivity, respectively. The total number of the generated electron-hole pairs per second in the simulated region in $\text{pairs} \cdot \text{s}^{-1}$ is given by

$$G(\lambda) = \iiint g(\lambda, x, y, z) dx dy dz \quad (2)$$

Then, $P_g(\lambda)$ can be calculated as the ratio of $G(\lambda)$ and the number of incident photons per second, $\Phi(\lambda)$, and written as

$$P_g(\lambda) = \frac{G(\lambda)}{\Phi(\lambda)} \quad (3)$$

The second step is the transport of the photo-generated electrons to the surface (process B in Fig. 1(b)), described by the probability of the electron being transported to the emission surface (P_t), which can be simulated by self-consistently solving the drift-diffusion equations of electrons

and holes use a full Newton's scheme [39]. A Cogenda Technology Computer-Aided Design (TCAD) tool was used for this simulation [38]. Figure 1(d) shows the TCAD setup, in which the bottom of the substrate was set as an Ohmic contact, and the emission surfaces were assigned charge emission boundary conditions. The electron transport current, $I_t(\lambda)$, was calculated by importing $g(\lambda, x, y, z)$ to the TCAD model, and then P_t was calculated as

$$P_t(\lambda) = \frac{I_t(\lambda)}{qG(\lambda)} \quad (4)$$

where q is the unit of elementary charge.

The third step is the emission of electrons into vacuum (process C in Fig. 1(b)) described by the surface-electron escape probability, P_e . Due to the C_S and F activation layer on the surface, the vacuum level is lowered below the bulk conduction band minima (NEA condition). Electrons reaching the surface tunnel through a small barrier formed by the activation layer and are emitted into vacuum. This tunneling process depends on the dopant concentration and the level of contamination of the photocathode surface. In Fig. 1(b), a downward band-bending occurs at GaAs surface, which affects the energy distribution of the photoelectrons in the conduction band and subsequently the surface-escape process. Two valley [36] and three valley [40] conduction band models have been used to analyze this process, which can accurately account for the dopant concentration. However, surface band-bending is difficult to model exactly because even small amounts of surface contamination can drastically impact the NEA condition. In this work, P_e was obtained by fitting the theoretical P_g and P_t to published QE spectra of flat wafer GaAs photocathode samples [34,36]. By combining these simulations, the emitted electron current, $I_e(\lambda)$, from the photocathode can be calculated as

$$I_e(\lambda) = I_t(\lambda) \times P_e(\lambda) \quad (5)$$

Finally, the photoelectron emission QE of the NEA photocathode can be calculated as

$$QE(\lambda) = \left| \frac{I_e(\lambda)}{q\Phi(\lambda)} \right| \times 100\% = P_g(\lambda) \times P_t(\lambda) \times P_e(\lambda) \quad (6)$$

Table 1 lists the optical and electrical parameters of GaAs photocathodes used in QE simulation.

Photoelectron emission processes are illustrated in Figs. 2(a) and 2(b) for the GaAs NPA and flat surface (referred to as flat wafer hereafter) photocathodes, respectively. From Fig. 2, we can see the advantages of NPA over flat wafer photocathodes in terms of key photocathode performance features. Light absorption in NPA can be much larger than flat wafer because the local density of optical states (LDOS) in nanopillars can be significantly enhanced by Mie resonance. And the photoelectrons can be highly localized inside the nanopillars near the top and side surfaces where the electrons can be efficiently transported and emitted to vacuum, which helps to increase P_g and P_t , and ultimately leads to the enhancement of QE .

The light scattering (σ_{sca}), absorption (σ_{abs}), and extinction cross-sections (σ_{ext}) can be used to analyze the Mie resonance properties which are defined as [41]

$$\sigma_{sca,abs,ext} = P_{sca,abs,ext} / I \quad (7)$$

where P_{sca} , P_{abs} , P_{ext} describe the scattered, absorbed and total extinction power by GaAs NPA in Watts, respectively, and I is the incident light intensity in Watts/ μm^2 . The LDOS enhancement in nanopillars can be expressed by considering the light concentration factor, C , defined as the ratio of the absorption cross-section (σ_{abs}) and the projected physical area (σ_{phy}) of the nanopillar.

For a NPA photocathode with surface area a , C can be written as [29]

$$C(\lambda) = \frac{\sigma_{abs}(\lambda)}{\sigma_{phy}} = \frac{\eta_a(\lambda) \times a}{f \times a} = \frac{\eta_a(\lambda)}{f} \quad (8)$$

where $\eta_a(\lambda)$ and f describe the light absorption spectra and array filling factor of the GaAs NPA, respectively.

For the evenly-spaced NPA with pillars oriented vertically on the substrate and the incident light propagating along the axis of the nanopillar, f can be calculated as

$$f = \frac{\pi}{4} \times \left(\frac{D}{P}\right)^2 \quad (9)$$

Table 1. GaAs photocathode material parameters used in simulations, taken from Refs. [39,42–44]

| Material | GaAs |
|---|---|
| Operational temperature, T | 300K |
| Refractive index (n) and extinction coefficient (k) | Taken from reference [42] |
| P -type doping concentration, N_A | $1 \times 10^{19} \text{ cm}^{-3}$ |
| Density of state, $N_{C,V}$ | $N_C = 4.7 \times 10^{17} \text{ cm}^{-3}$, $N_V = 9 \times 10^{18} \text{ cm}^{-3}$ [43] |
| Intrinsic electron density, n_i | $n_i = 2.1 \times 10^6 \text{ cm}^{-3}$ [43] |
| Radiative recombination coefficient, B | $B = 1.8 \times 10^{-10} \text{ cm}^3 \text{ s}^{-1}$ [39] |
| Auger recombination coefficient, C_e, C_h | $C_e = 7 \times 10^{-32} \text{ cm}^6 \text{ s}^{-1}$, $C_h = 6.1 \times 10^{-31} \text{ cm}^6 \text{ s}^{-1}$ [39] |
| SRH recombination lifetime, τ_{e0}, τ_{h0} | $\tau_{e0} = \tau_{h0} = 10^{-7} \text{ s}$ [39] |
| Surface recombination velocities, S_e, S_h | $S_e = S_h = 10^4 \text{ cm} \cdot \text{s}^{-1}$ [39] |
| ^a Electron and hole mobility, $\mu_{e,h}$ | $\mu_e (N_A = 1 \times 10^{19} \text{ cm}^{-3}, T = 300 \text{ K}) \approx 1546 \text{ cm}^2 \text{ V}^{-1} \text{ s}^{-1}$ $\mu_h (N_A = 1 \times 10^{19} \text{ cm}^{-3}, T = 300 \text{ K}) \approx 99 \text{ cm}^2 \text{ V}^{-1} \text{ s}^{-1}$ [44] |
| ^b Electron diffusion length, L_e | $L_e = (D_e \tau_e)^{0.5} \approx 1500 \text{ nm}$ |

^a μ_e and μ_h are calculated by the Caughey–Thomas model [44].

^a D_e is the electron diffusion coefficient calculated by $D_e = (\mu_e \cdot k \cdot T)/q$, where k , q , and T are the Boltzmann constant, the unit of elementary charge and temperature, respectively. τ_e is the total bulk electron lifetime by considering the radiative, Auger and SRH recombination mechanisms as listed in table.

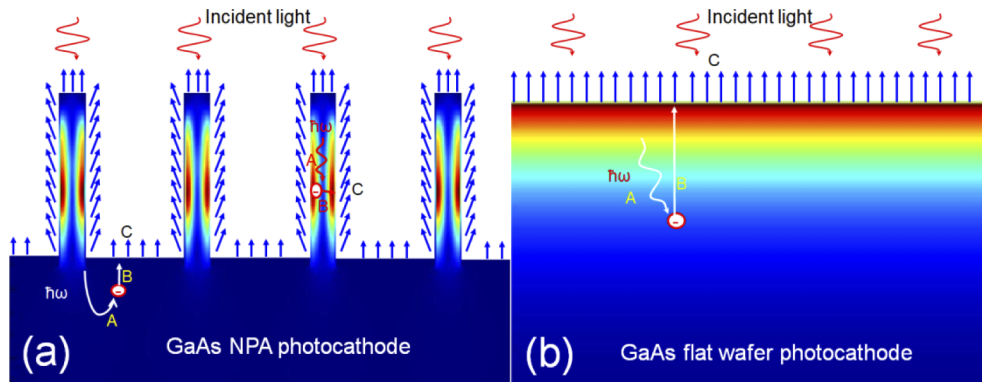


Fig. 2. Electron emission processes in GaAs photocathodes. (a) GaAs NPA photocathode, (b) GaAs flat wafer photocathode.

and σ_{phy} is equal to the cross sectional area of nanopillar and can be calculated as

$$\sigma_{phy} = \frac{\pi}{4} \times D^2 \quad (10)$$

Furthermore, the NPA photocathode has a larger effective electron emission area, a_{NPA} , compared to a flat wafer, a_{flat} , due to the fact that the electrons are emitted from both the top and side surfaces of nanopillars, which also permits larger QE . For the evenly-spaced NPA, the ratio of a_{NPA} to a_{flat} , defined as r_{emi} , provides a measure of the effective electron emission surface area enhancement and can be calculated by

$$r_{emi} = a_{NPA}/a_{flat} = 1 + \frac{\pi DH}{P^2} \quad (11)$$

For typical NPA photocathodes described here, surface area enhancement by a factor of 3 can be easily achieved.

It's worth noting that, since the diameter and height of the GaAs nanopillars investigated in this paper are larger than 100 nm, the quantum confinement effect can be neglected. The optoelectronic model we employed here, combining the wave optics properties of the light-matter interaction with coupled drift-diffusion equations for the electrons and holes, has been widely used to describe the optoelectronic and carrier transportation properties of the optoelectronic devices with the nanostructures similar to this work [45–46].

3. Results and discussion

3.1. Optical design of Mie-type GaAs NPA resonators for NEA photocathodes

To achieve the desired QE enhancement, the optical structure of NPA must be optimized for maximum light absorption at a specific wavelength. Systematic studies on the Mie resonant properties of Si nanopillars have been reported, however, similar work has not been performed with GaAs. As shown in Fig. 3(a), at 400 ~ 900 nm wavelength (λ) range, GaAs and Si have similar refractive index n , but the light extinction coefficient k of GaAs is significantly higher. Figure 3(b) shows the cross-sectional spectra calculated by FDTD for GaAs and Si nanopillar arrays on respective substrates, with pillar diameter $D = 100$ nm and pillar height $H = 100$ nm, with resonant peaks observed at $\lambda \sim 518$ nm for both materials. It can be seen that σ_{abs} is more than 2 times larger than σ_{phy} for GaAs nanopillar at the resonance peak (e.g. $C > 2$), and is much larger than that of Si due to much larger k of GaAs. This means photons are more readily absorbed in GaAs within the 500 ~ 800 nm waveband, i.e. every absorbed photon can generate an electron-hole pair and contribute to the generation of photoelectron current from NEA photocathodes. Figures 3(c) and 3(d) present the normalized electric/magnetic field intensity ($|E|^2/|H|^2$) profiles and field lines in vertical crosscuts through the center of a GaAs nanopillar around $\lambda \sim 518$ nm, which clearly show the loops induced by the driving electric/magnetic field also drive the Mie-type magnetic/electric dipole resonance modes (MD/ED). The MD enhanced $|H|^2$ and ED enhanced $|E|^2$ are also shown in Figs. 3(e) and 3(f), respectively, which clearly indicate the enhanced LDOS in nanopillars.

Mie resonances depend on the NPA geometry parameters. An FDTD analysis was used to model the light absorption efficiency, η_a , and light concentration, C , of GaAs NPAs as a function of the geometric parameters and the wavelength λ of the plane-wave radiation propagating along the nanopillar axes. For lattice period $P = 600$ nm, Figs. 4(a) and 4(b) give the dependence of η_a spectra on pillar diameter D for pillar heights $H = 350$ nm and 750 nm, respectively. The NPA filling factors, f , are also shown in the figures and were used to calculate the light concentration coefficient C . Some dominant η_a spectral branches are observed in Figs. 4(a) and 4(b), and agree with Mie's resonant theory [20], namely, the lowest-order magnetic/electric dipole (MD/ED) mode is excited when $(Dn)/\lambda = 1$, whereas the quadrupole (MQ/EQ) and higher-order multipole

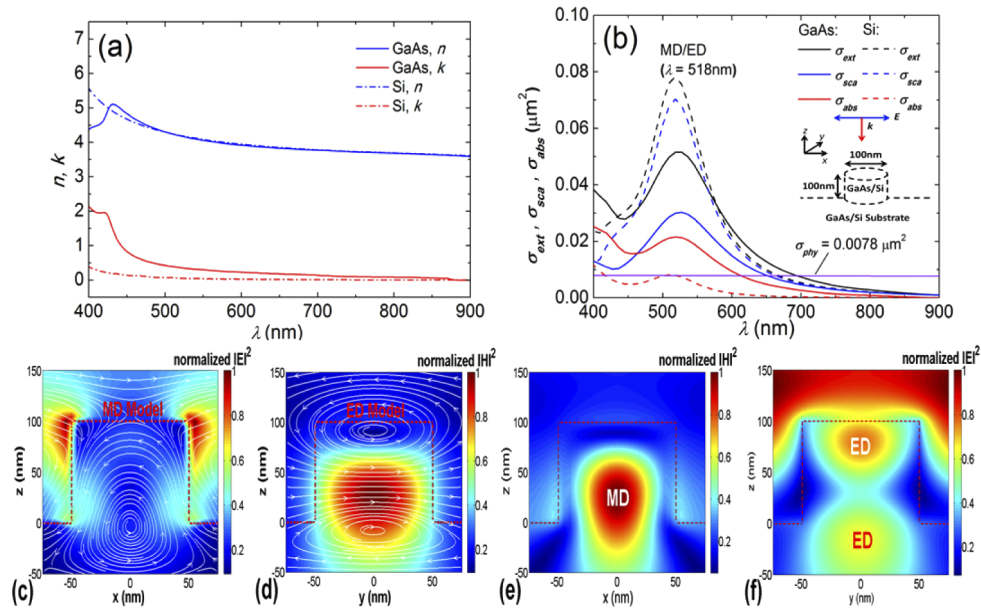


Fig. 3. Mie resonance characteristics of GaAs and Si nanopillars on substrate. (a) Refractive index, n , and extinction coefficient, k , of GaAs and Si vs. wavelength (λ) from 400 to 900 nm, the data is adopted from Ref. [42]. (b) Cross-section (σ_{scat} , σ_{abs} , σ_{ext}) spectra of GaAs and Si nanopillars on respective substrates, the parameters of incident light and geometry are shown as insets. (c)–(d) Normalized electric and magnetic field intensity ($|E|^2$ and $|H|^2$, colored) and field lines (white) in vertical crosscuts through the center of the GaAs nanopillar at the resonance wavelength $\lambda \sim 518$ nm. (e)–(f) The same crosscuts as in c and d, but showing the resonance enhanced $|H|^2$ and $|E|^2$ (colored), respectively. The magnetic and electric dipole (MD and ED) resonance modes are labeled in (e) and (f), respectively.

modes are excited for larger values of $(Dn)/\lambda$ which are labeled as the corresponding η_a peaks. Figures 4(c)–4(f) give the $|E|^2/|H|^2$ profiles and field lines of dipole (black dot $M1$ in Fig. 4(a)) and quadrupole (black dot $M2$ in Fig. 4(a)) modes, which confirm the Mie-type resonance modes for the corresponding η_a peaks.

By comparing Figs. 4(a) with 4(b), the same resonance modes are excited in both photocathodes at similar values of D . And for both cases, the dipole modes are excited by the smallest D , and therefore can provide the largest C . The pillar height H has the most profound impact, with stronger absorption resonance peaks obtained by increasing pillar height H . This can be understood from Figs. 4(g)–4(j), which show the MD and MQ enhanced $|H|^2$ profiles in vertical crosscuts parallel to the driving electric field through the center of GaAs nanopillars $M1$, $M2$, $M3$, and $M4$ (indicated by black dots in Figs. 4(a) and 4(b)). As can be seen, a much larger fraction of $|H|^2$ can be coupled into taller nanopillars, giving rise to increased η_a in nanopillars. A similar argument holds for the ED and EQ modes.

From Fig. 4, the dipole and quadrupole resonance-dominated η_a absorption spectra branches cover the wavelength range 500 ~ 850 nm, consistent with photoelectron emission requirements of GaAs photocathodes. The largest C , and potentially the strongest QE enhancement, can be achieved in MD/ED resonance mode. For a practical GaAs NEA photocathode electron gun, a typical operating wavelength is 532 nm for un-polarized electron beam [7,9–11,34] and 780 nm for spin-polarized beam [8,47–48]. Figure 4 shows that GaAs NPAs with D of 100 nm and 160 nm can excite dipole resonance at ~532 nm and ~780 nm, respectively. Figure 5 explores the

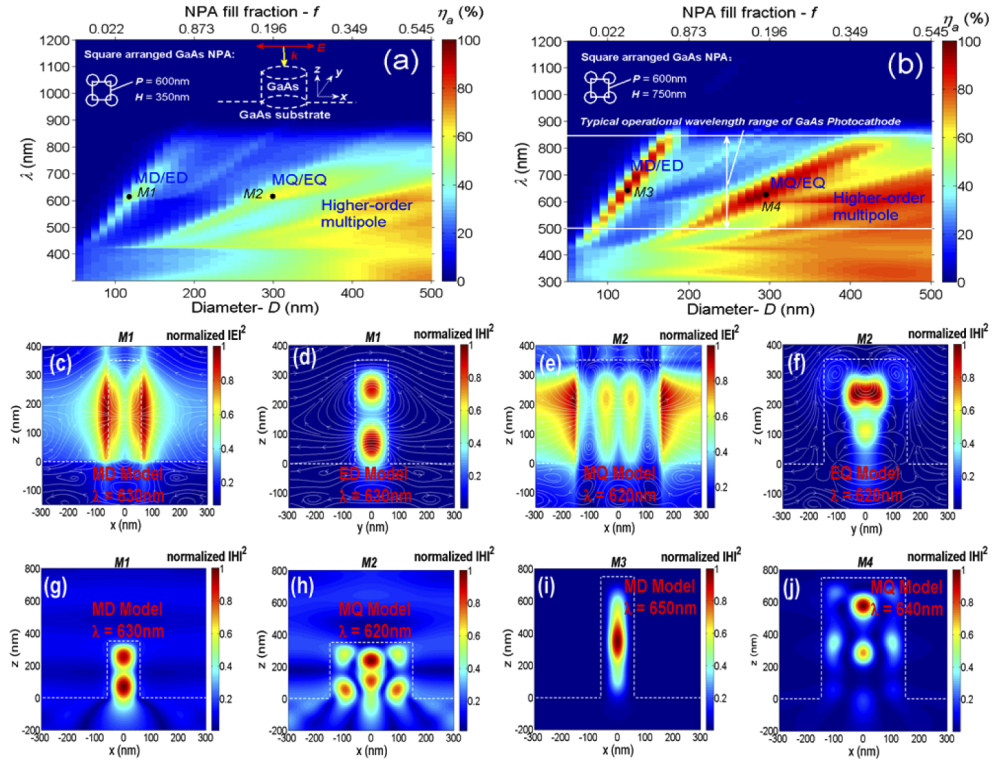


Fig. 4. Mie resonance enhanced light absorption in GaAs NPA. (a), (b) dependence of η_a (color) absorption spectra on diameter- D for GaAs NPA with $H = 350$ nm and 750 nm, respectively. The incident light and geometry parameters are shown as insets. The black dots $M1$ ($D = 120$ nm), $M2$ ($D = 300$ nm), $M3$ ($D = 120$ nm), $M4$ ($D = 300$ nm) correspond to wavelength λ and geometry combinations used for (c) - (j). (c)/(d) and (e)/(f) are the normalized $|E|^2/|H|^2$ (color) and field lines (white) in vertical crosscuts through the center of the nanopillars $M1$ (MD/ED resonance at 630 nm) and $M2$ (MQ/EQ resonance at 620 nm), respectively. (g) - (j) are the resonance enhanced $|H|^2$ (color) for $M1$ (MD at 630 nm), $M2$ (MQ at 620 nm), $M3$ (MD at 650 nm) and $M4$ (MQ at 640 nm).

dependence of dipole resonance enhanced absorption, η_{a-res} , and resonance wavelength, λ_{res} , on P and H for these two types of GaAs NPAs.

It can be seen from Fig. 5 that λ_{res} barely changes with P , whereas η_{a-res} appears quite sensitive to P . Increasing P decreases f and light coupling in nanopillars and significantly weakens η_{a-res} . However, stronger light coupling can be achieved with taller nanopillars which allow larger P for the highest η_{a-res} and also larger light concentration C due to smaller f . With respect to NPA in Fig. 5(a) with $D = 100$ nm, $H = 700$ nm and $P = 300 \sim 400$ nm, nearly 100% η_{a-res} is obtained at $\lambda_{res} \sim 532$ nm, and the corresponding light concentration values, C , are between 11 and 20. However, for the NPA of Fig. 5(b) with $D = 160$ nm, a maximum η_{a-res} of only about 95% is obtained at $\lambda_{res} \sim 780$ nm with $P = 500$ nm and much larger $H = 1200$ nm, and the corresponding C is about 12. This means much taller pillars are needed to fully concentrate and absorb the light at longer wavelengths in nanopillars due to the decreased light extinction coefficient, k , of GaAs (see in Fig. 3(a)), which increases the difficulty of NPA fabrication. However, light concentration and absorption enhancement at longer wavelengths has special meaning for certain practical electron source applications as discussed in the following section.

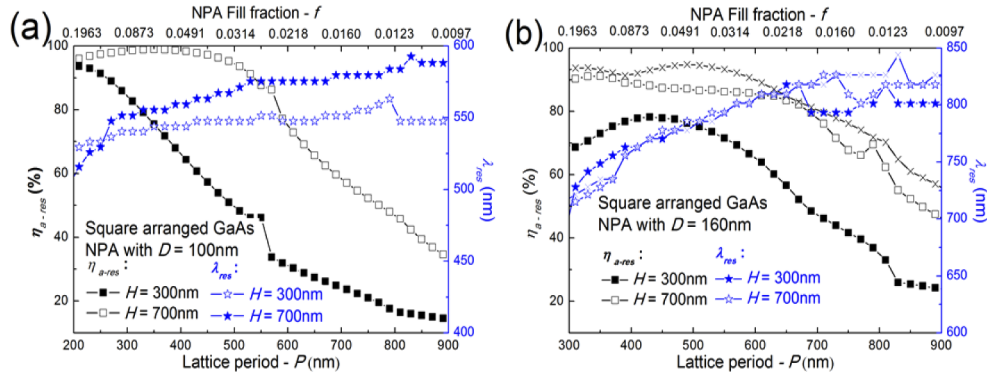


Fig. 5. Dependence of the dipole resonance enhanced light absorption and resonance wavelength upon lattice period, P , and pillar height, H , of evenly-spaced GaAs NPA. (a) $D = 100$ nm. (b) $D = 160$ nm.

The analysis above serves to inform the optical design philosophy to achieve the largest QE enhancement in NPA photocathodes. Namely, for a practical NPA photocathode operating at a specified wavelength, the nanopillar diameter, D , was selected to excite the corresponding resonance mode, with the nanopillar height, H , chosen to be tall enough to fully absorb the incident light and the lattice period, P , selected to balance the light concentration and the electron emission area of the nanopillars (see in Eq. (10)).

3.2. Enhanced QE from GaAs NPA resonator photocathodes

Photoelectron emission processes in GaAs NPA photocathodes were analyzed based on the theoretical models and material parameters shown in section 2. From Eq. (6), QE was calculated as the product of P_g , P_t and P_e . The quantities P_g and P_t were simulated using FDTD and TCAD tools, respectively while P_e was obtained by fitting the theoretical P_g and P_t to published QE spectra of a GaAs “epi-ready” flat wafer photocathode over the wavelength range 500 ~ 800 nm [34]. The results are shown in Fig. 6 which indicates QE is primarily limited by P_e (i.e., the smallest of the three quantities). But note that P_e is still approximately twice as large as the measured QE across the entire wavelength range, indicating there is considerable opportunity for improving QE via P_g and P_t , which can be done by NPA resonators.

It is possible for electrons to be emitted from the nanopillar surfaces and the substrate of the GaAs NPA photocathode, although for this application, the intent is for electrons to emit only from the nanopillars. Electrons emitted from nanopillars and the substrate were simulated and analyzed separately as illustrated in Fig. 7(a). Some photoelectrons might be transported between pillar and substrate, but this contribution is considered to be small and as such, it was ignored in the model. Since no experimental QE data of nano-structured photocathode is available, the fitted P_e from Fig. 6 was used to calculate QE of the investigated GaAs NPA and flat wafer photocathodes. Based on the optical design consideration described in section 3.1 and the targeted operation at specific wavelengths, GaAs NPA photocathodes with MD/ED resonance wavelengths at ~532 nm ($D = 100$ nm, $H = 700$ nm, $P = 300$ nm, labeled as $N1$) and ~780 nm ($D = 160$ nm, $H = 1200$ nm, $P = 500$ nm, labeled as $N2$) were analyzed.

Figure 7(b) presents the simulated surface reflectance spectra for these two NPAs together with flat wafer results (labeled as W) within the 400 ~ 900 nm waveband. The reflectance of flat wafer was greater than 30% across the entire waveband, whereas the reflectance of $N1$ and $N2$ were only ~1% at the MD/ED resonance wavelengths of ~532 nm and ~780 nm, respectively. With such ultralow reflectance, the NPA photocathode can be considered an optically “dark” photocathode.

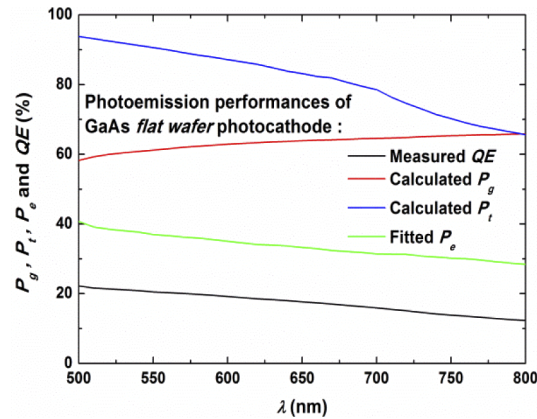


Fig. 6. Fitted P_e from GaAs “epi-ready” flat wafer photocathode: QE (black line) was measured in a previous report [34], P_g (red line) and P_t (blue line) were simulated using the FDTD and TCAD tools, respectively, P_e (green line) was then obtained by fitting P_g and P_t to measured QE data.

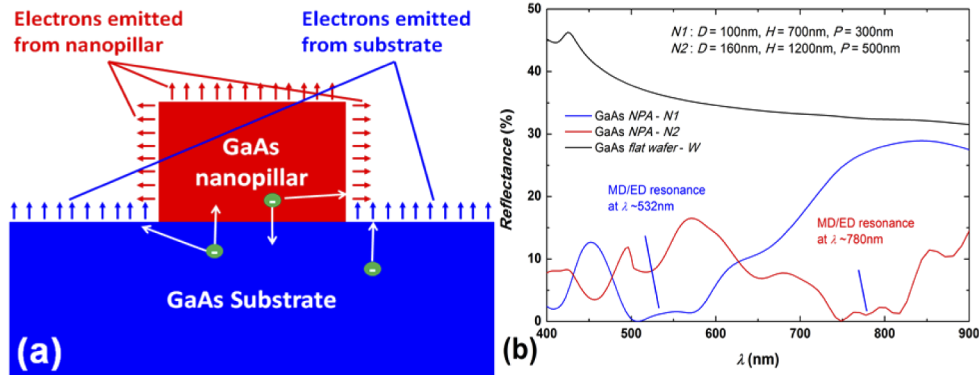


Fig. 7. (a) Cross-section illustration of electron emission from nanopillar and substrate of GaAs NPA photocathode. (b) Simulated surface reflectance spectra for GaAs NPA (labeled as $N1$, $N2$) and flat wafer (labeled as W) in the 400 ~ 900 nm waveband.

Reduced reflectance is a very useful feature for DC high voltage photoguns. Reflection of the incident laser light from the photocathode surface leads to unwanted/unintended photoemission from the edge of the photocathode producing electron beam that is not properly transported from the photogun. This unintended photoemission strikes the vacuum chamber walls, degrading vacuum and hastening photocathode QE decay and leading to accelerator downtime [15]. GaAs NPA photocathodes and NPA coatings applied to the photogun vacuum chamber walls could significantly improve the operating lifetime of the photogun.

Simulated photocathode QE spectra of GaAs NPAs $N1$ and $N2$ together with flat wafer in 500 ~ 800 nm wavelength range are presented in Figs. 8(a) and 8(b), respectively. It clearly shows that QE is enhanced by NPA resonators. Since the same P_e was used for NPA and flat wafer, this enhancement is mainly due to P_g and P_t presented in Figs. 8(c) and 8(d), respectively.

The photoemission performance represented by P_g , P_t and QE for the nanopillar and substrate of NPA photocathodes in Fig. 8 make it possible to analyze the contributions from nanopillar and substrate separately. For GaAs NPA photocathodes $N1$ and $N2$, a P_t of nearly 100% nanopillars can be obtained across the entire 500 ~ 800 nm waveband (see Fig. 8(d)), indicating excellent

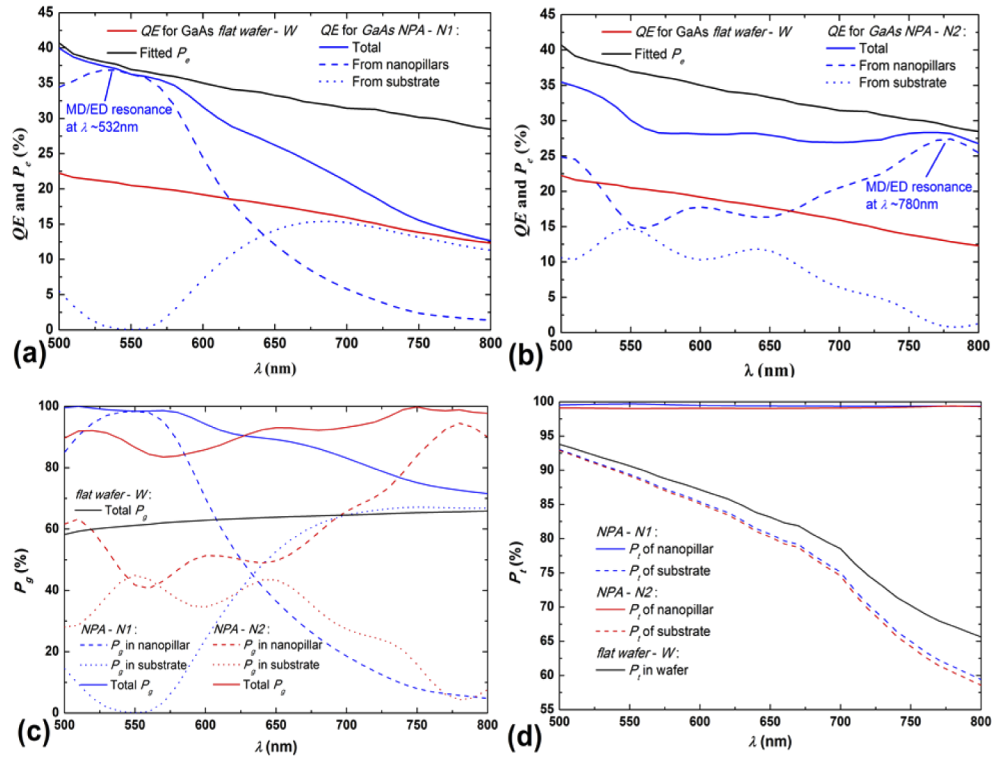


Fig. 8. Simulated QE and related performances of GaAs photocathodes. Simulated total QE (solid blue line) and QE from nanopillars (dashed blue line) and substrate (dotted blue line) for (a) GaAs NPA photocathodes N1 ($D = 100$ nm, $H = 700$ nm, $P = 300$ nm), (b) N2 ($D = 160$ nm, $H = 1200$ nm, $P = 500$ nm). The QE and fitted P_e of GaAs flat wafer (W) photocathode are also presented as solid red and black lines in (a) and (b) for comparison. (c-d) Simulated P_g and P_t of N1 (blue lines), N2 (red lines) and GaAs flat wafer (black line) photocathodes.

photoelectron transport properties of nanopillars due to their much smaller transport distances compared to flat wafers as mentioned in section 2 (see Fig. 2). However, photoelectrons in the substrate need to be transported to the surface free of nanopillars, or through a nanopillar, to be emitted into vacuum. This increases the effective transport distance and therefore reduces P_t compared to the flat wafer, as seen in Fig. 8(d). So, it is necessary to decrease the surface reflectance and fully absorb the incident light inside the nanopillars to enhance QE as much as possible. Theoretical results show P_g of nearly 99% for NPA photocathode sample N1 and 95% for sample N2, exciting peak MD/ED resonances at wavelengths 532 nm and 780 nm (see Fig. 8(c)), respectively. In addition, nearly 100% P_t is obtained from pillars at these two wavelengths (see Fig. 8(d)), which leads to QE enhancement of factors 1.8 for N1 and 2.2 for N2 compared to the flat wafer photocathode (see Fig. 8(a)).

These data indicate larger resonance QE enhancement is achieved for N2 even with a smaller P_g at $\lambda \sim 780$ nm compared to sample N1 at ~ 532 nm. This can be explained by excellent electron transport properties of nanopillars. Similar to other optoelectronic devices such as photovoltaic solar cells [27–33], photoelectrons in photocathodes are transported to the surface through the diffusion process. The electron diffusion length, L_e , which is ~ 1500 nm for GaAs with p -type doping concentration of $1 \times 10^{19} \text{ cm}^{-3}$ as shown in Table 1, can be used to evaluate the transport properties of the photoelectrons. Based on the optical constants in Fig. 3(a), the GaAs thickness

needed to absorb $\sim 95\%$ of the incident light (referred to hereafter as the absorption depth, D_a) was calculated to be ~ 450 nm at 532 nm, and ~ 2500 nm at 780 nm. When the absorption depth is much longer than the diffusion length, as is the case for 780 nm light, the photoelectrons are not transported as efficiently to the surface due to carrier recombination, which causes decreased P_t for the GaAs flat wafer photocathode as observed in Fig. 8(d). But this is not such a problem for NPAs, where light can be concentrated near the surface. A pillar height of 1200 nm is needed for N_2 to absorb $\sim 95\%$ of the incident light ($\lambda \sim 780$ nm) and the P_t of nanopillar does not decrease with wavelength due to the fact that the photoelectrons can be emitted from the pillar side surfaces. These different wavelength dependent properties of P_t for nanopillars and flat wafers lead to the intensified enhancement of P_t and QE by NPAs as wavelength becomes longer as observed in Fig. 8. As mentioned in section 3.1, stronger enhancement on photocathode QE at long wavelengths bears special implication for certain practical electron source applications. Namely, the highest electron spin polarization can be obtained at $\lambda \sim 780$ nm for GaAs photocathode [47–48]. In addition, the mean transverse energy of the electron emission can be effectively suppressed at long wavelengths near band edge ($\lambda \sim 850$ nm), which may lead to lower thermal emittance of the electron beams [9,16,40].

To better understand the impact of enhanced light concentration, we introduce QE_{nor} , which stands for the nanopillar QE normalized by the projected physical area, as reported in Refs. [29–33]. Specifically, QE_{nor} was calculated by considering only the incident photons projected onto the physical area of nanopillars. Figure 9(a) presents the calculated QE_{nor} spectra, it can be seen that the QE_{nor} of two nanopillars (N_1 and N_2) extends to 420% and 340% at the MD/ED resonance wavelengths of 532 nm and 780 nm, respectively, which further confirms the strong light concentration ability of NPA resonators. Note here, QE_{nor} can exceed 100% because the actual absorbed light power is greater than the projected light power within the nanopillars, which should not be confused with the classic definition of QE that is the ratio of number of electrons to the number of absorbed photons. The impact of the MD/ED resonance enhanced light concentration upon the distribution of the photoelectron generation rate in NPAs is shown in Fig. 9(b), clearly the photo generation rates are concentrated near the sides of the nanopillars for both N_1 and N_2 . This means most of the photoelectrons can be transported efficiently to side surfaces of the nanopillars, which not only improves P_t and enhances QE as discussed before, but also decreases the electron transport time due to the shortened transport distance, which can be potentially very useful in applications such as ultrafast photoemission.

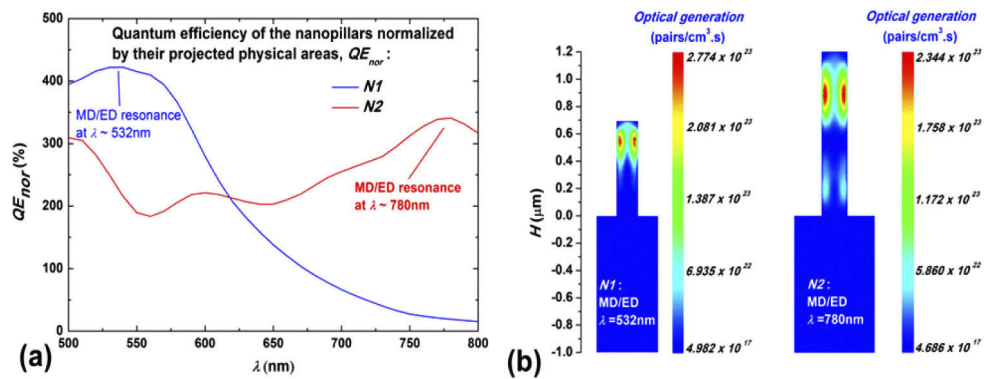


Fig. 9. Impact of resonance enhanced light concentration on the photoelectric properties of the NPA photocathodes. (a) QE_{no} (see definition in the text) for NPA photocathodes N_1 and N_2 . (b) Distribution of photoelectron generation rate in pairs. $\text{cm}^{-3}\text{s}^{-1}$ within the vertical cross section of the samples N_1 and N_2 in the plane parallel to the E-field of the linearly polarized incident light at the resonance wavelengths. Light intensity is 0.1Wcm^{-2} .

As a final assessment of the NPA photocathode described above, the performance at the resonance wavelengths are summarized in Table 2. We can see P_g and P_t of the nanopillars can be enhanced to nearly 100%, resulting in the QE enhancement by a factor of 1.8 for NPA sample $N1$ at the resonance wavelength of 532 nm, and by a factor of 2.2 at 780 nm for NPA sample $N2$, compared to the flat wafer photocathodes. Some accelerator applications benefit from electron beams with small thermal emittance. For these applications, the GaAs NPA provides a way to operate at the bandgap, to obtain small emittance, with a high QE that is typically only obtained by operating at shorter wavelengths. It is also worth considering that P_e can also be improved by increased thermal electron emissions [36,40,49] at shorter wavelengths due to the increased electron emission area of the NPA, which represents future study using experimental data to be obtained from practical NPA photocathodes. In this work, the r_{emi} , which provides a measure of the effective electron emission area enhancement of NPA, was calculated by Eq. (11) and listed in Table 2 for references.

Table 2. Photoemission performance parameters of GaAs NPA and flat wafer photocathodes at the resonance wavelengths (λ_r)

| Photocathode | λ_r | Material | Calculated P_g (%) | Calculated P_t (%) | Fitted P_e (%) | Calculated r_{emi} | Calculated QE (%) |
|-----------------|-------------|------------|----------------------|----------------------|------------------|----------------------|---------------------|
| NPA: $N1$ | 532nm | nanopillar | 97.07 | 99.66 | 38.07 | 3.44 | 36.83 |
| | | substrate | 1.89 | 90.81 | 38.07 | | 0.65 |
| flat wafer: W | 532nm | flat wafer | 60.41 | 91.86 | 38.07 | 1.00 | 21.13 |
| NPA: $N2$ | 780nm | nanopillar | 94.51 | 99.37 | 29.19 | 3.41 | 27.41 |
| | | substrate | 4.36 | 60.48 | 29.19 | | 0.77 |
| flat wafer: W | 780nm | flat wafer | 65.64 | 67.20 | 29.19 | 1.00 | 12.87 |

4. Conclusions

We presented studies on a new type of NEA photocathode with enhanced photoemission performances by patterning the photocathode surface with GaAs NPA Mie-type resonant structures. Large resonance-enhanced absorption can be achieved in GaAs nano-pillars due to the large absorption coefficient of direct-bandgap GaAs, which allows strong localization of the photoelectrons near the top and sides of the nanopillars surfaces where electrons can be efficiently transported and emitted into vacuum, resulting in significant photocathode QE enhancement. Mie-type resonance modeling of GaAs NPAs shows that resonance conditions can be obtained over the entire 500 ~ 850 nm waveband by adjusting pillar diameter, height and spacing, thereby satisfying the requirements of most photocathode applications. This paper described NPA designs that provide strong dipole resonances at wavelengths 532 nm and 780 nm, to support un-polarized and polarized photoemission applications. The spectrally-resolved photoemission predictions based on Spicer's three-step model show that these structures, when properly optimized, provide QE limited only by the surface-electron escape probability and significantly outperform traditional flat wafer photocathodes.

Besides the QE enhancement, the ultralow surface reflectance ($\sim 1\%$) of these NPA photocathodes clearly indicates the use of NPA can be a very effective measure for suppressing unwanted photoemission to improve the operating lifetime of DC high voltage photoguns. An ultrashort photoelectric response can be also expected due to the much shorter photoelectron transportation distance in nanopillar than in flat wafer. The only functional part of the semiconductor NPA photocathode is the p -doped GaAs NPA, which can be directly fabricated on substrates using inexpensive industrial fabrication processes such as nanoimprint lithography. We believe these nanostructured GaAs resonators are very promising materials that could significantly improve the photoemission efficiency and photoelectric response of NEA photocathodes to meet the stringent

requirements by applications such as high-resolution spectral low-light-level imaging and large scale electron accelerator applications. Due to the limitation of the present simulation method, some practical issues related to the cathode activation such as surface roughness and shading effect from Cs deposition, lifetime due to the backward ion bombardment can't be addressed in this paper, but will be interesting subjects to pursue in future research, in particular experimental studies.

Funding

National Natural Science Foundation of China (11875012, 61204071, 61661002); U.S. Department of Energy (DE-AC05-06OR23177).

Disclosures

The authors declare no conflicts of interest.

References

1. L. Conti, J. Barnstedt, L. Hanke, C. Kalkuhl, N. Kappelmann, T. Rauch, B. Stelzer, K. Werner, H. Elsener, and D. M. Schadt, "MCP detector development for UV space missions," *Astrophys. Space Sci.* **363**(4), 63 (2018).
2. J. Wehmeier and B. van Geest, "High-speed imaging: Image intensification," *Nat. Photonics* **4**(3), 152–153 (2010).
3. G. Tang, F. Yan, X. Chen, and W. Luo, "High-quantum-efficiency ultraviolet solar-blind AlGaIn photocathode detector with a sharp spectral sensitivity threshold at 300 nm," *Appl. Opt.* **57**(27), 8060–8064 (2018).
4. J. Zou, X. Ge, Y. Zhang, W. Deng, Z. Zhu, W. Wang, X. Peng, Z. Chen, and B. Chang, "Negative electron affinity GaAs wire-array photocathodes," *Opt. Express* **24**(5), 4632–4639 (2016).
5. C. Feng, Y. Zhang, Y. Qian, J. Liu, J. Zhang, F. Shi, X. Bai, and J. Zou, "Improved quantum efficiency and stability of GaAs photocathode using favorable illumination during activation," *Ultramicroscopy* **202**, 128–132 (2019).
6. Y. Zhang, Y. Qian, C. Feng, F. Shi, H. Cheng, J. Zou, J. Zhang, and X. Zhang, "Improved activation technique for preparing high-efficiency GaAs photocathodes," *Opt. Mater. Express* **7**(9), 3456–3465 (2017).
7. N. A. Moody, K. L. Jensen, A. Shabaev, S. G. Lambrakos, J. Smedley, D. Finkenstadt, J. M. Pietryga, P. M. Anisimov, V. Pavlenko, E. R. Batista, J. W. Lewellen, F. Liu, G. Gupta, A. Mohite, H. Yamaguchi, M. A. Hoffbauer, and I. Robe, "Perspectives on Designer Photocathodes for X-ray Free-Electron Lasers: Influencing Emission Properties with Heterostructures and Nanoengineered Electronic States," *Phys. Rev. Appl.* **10**(4), 047002 (2018).
8. D. Abbott, P. Adderley, A. Adeyemi, P. Aguilera, M. Ali, H. Areti, M. Baylac, J. Benesch, G. Bosson, B. Cade, A. Camsonne, L. S. Cardman, J. Clark, P. Cole, S. Covert, C. Cuevas, O. Dadoun, D. Dale, H. Dong, J. Dumas, E. Fanchini, T. Forest, E. Forman, A. Freyberger, E. Froidefond, S. Golge, J. Grames, P. Guèye, J. Hansknecht, P. Harrell, J. Hoskins, C. Hyde, B. Josey, R. Kazimi, Y. Kim, D. Machie, K. Mahoney, R. Mammei, M. Marton, J. McCarter, M. McCaughan, M. McHugh, D. McNulty, K. E. Mesick, T. Michaelides, R. Michaels, B. Moffit, D. Moser, C. Muñoz Camacho, J.-F. Muraz, A. Oppen, M. Poelker, J.-S. Réal, L. Richardson, S. Setiniyaz, M. Stutzman, R. Suleiman, C. Tennant, C. Tsai, D. Turner, M. Ungaro, A. Variola, E. Voutier, Y. Wang, and Y. Zhang, "Production of Highly Polarized Positrons Using Polarized Electrons at MeV Energies," *Phys. Rev. Lett.* **116**(21), 214801 (2016).
9. S. Karkare, L. Boulet, L. Cultrera, B. Dunham, X. Liu, W. Schaff, and I. Bazarov, "Ultrabright and Ultrafast III–V Semiconductor Photocathodes," *Phys. Rev. Lett.* **112**(9), 097601 (2014).
10. R. Xiang and J. Teichert, "Photocathodes for High Brightness Photo Injectors," *Phys. Procedia* **77**, 58–65 (2015).
11. D. Wu, M. Li, X. Yang, H. Wang, X. Luo, X. Shen, D. Xiao, J. Wang, P. Li, X. Li, K. Zhou, C. Lao, Y. Xu, P. Zhang, L. Yan, S. Lin, Q. Pan, L. Shan, T. He, W. Bai, L. Yang, D. Deng, H. Zhang, J. Liu, Y. Chen, and D. Feng, "First Lasing of the CAEP THz FEL Facility Driven by a Superconducting Accelerator," *J. Phys.: Conf. Ser.* **1067**, 032010 (2018).
12. B. Liao and E. Najafi, "Scanning Ultrafast Electron Microscopy: A Novel Technique to Probe Photocathode Dynamics with High Spatial and Temporal Resolutions," *Mater. Today Phys.* **2**, 46–53 (2017).
13. T. Oshima, "NEA photocathode for SEM application," *Microelectron. Eng.* **67–68**, 951–954 (2003).
14. J. E. Schneider, P. Sen, D. S. Pickard, G. I. Winograd, M. A. McCord, R. F. W. Pease, and W. E. Spicer, "Patterned negative electron affinity photocathodes for maskless electron beam lithography," *J. Vac. Sci. Technol., B: Microelectron. Process. Phenom.* **16**(6), 3192–3196 (1998).
15. C. Hernandez-Garcia, M. Poelker, and J. Hansknecht, "High Voltage Studies of Inverted-geometry Ceramic Insulators for a 350 kV DC Polarized Electron Gun," *IEEE T. Dielect. El. In.* **23**(1), 418–427 (2016).
16. A. Shornikov, D. A. Orlov, C. Krantz, A. S. Jaroshevich, and A. Wolf, "Maximum intensity, transmission limited cold electron beams from GaAs photocathode in the eV and sub-eV kinetic energy range," *Phys. Rev. Spec. Top.-Accel. Beams* **17**(4), 042802 (2014).
17. J. Zou, W. Zhao, X. Ding, Z. Zhu, W. Deng, and W. Wang, "Spectral sensitivity of graded composition AlGaAs/GaAs nanowire photodetectors," *Appl. Phys. A* **122**(12), 1003 (2016).

18. C. Feng, Y. Zhang, Y. Qian, B. Chang, F. Shi, G. Jiao, and J. Zou, "Photoemission from advanced heterostructured Al_xGa_{1-x}As/GaAs photocathodes under multilevel built-in electric field," *Opt. Express* **23**(15), 19478–19488 (2015).
19. W. Liu, Y. Chen, W. Lu, A. Moy, M. Poelker, M. Stutzman, and S. Zhang, "Record-level quantum efficiency from a high polarization strained GaAs/GaAsP superlattice photocathode with distributed Bragg reflector," *Appl. Phys. Lett.* **109**(25), 252104 (2016).
20. A. I. Kuznetsov, A. E. Miroshnichenko, M. L. Brongersma, Y. S. Kivshar, and B. Luk'yanchuk, "Optically resonant dielectric nanostructures," *Science* **354**(6314), aag2472 (2016).
21. S. Jahani and Z. Jacob, "All-dielectric metamaterials," *Nat. Nanotechnol.* **11**(1), 23–36 (2016).
22. Y. Kivshar and A. Miroshnichenko, "Meta-Optics with Mie Resonances," *Opt. Photonics News* **28**(1), 24–31 (2017).
23. S. Kruk and Y. Kivshar, "Functional Meta-Optics and Nanophotonics Governed by Mie Resonances," *ACS Photonics* **4**(11), 2638–2649 (2017).
24. P. Spinelli, M. A. Verschuuren, and A. Polman, "Broadband omnidirectional antireflection coating based on subwavelength surface Mie resonators," *Nat. Commun.* **3**(1), 692 (2012).
25. L. Cao, P. Fan, A. P. Vasudev, J. S. White, Z. Yu, W. Cai, J. A. Schuller, S. Fan, and L. Mark, "Semiconductor nanowire optical antenna solar absorbers," *Nano Lett.* **10**(2), 439–445 (2010).
26. J. van de Groep and A. P. Center, "Designing dielectric resonators on substrates: Combining magnetic and electric resonances," *Opt. Express* **21**(22), 26285–26302 (2013).
27. Z. Gu, P. Prete, N. Lovergine, and B. Nabet, "On optical properties of GaAs and GaAs/AlGaAs core-shell periodic nanowire arrays," *J. Appl. Phys.* **109**(6), 064314 (2011).
28. L. Wen, Z. Zhao, X. Li, Y. Shen, H. Guo, and Y. Wang, "Theoretical analysis and modeling of light trapping in high efficiency GaAs nanowire array solar cells," *Appl. Phys. Lett.* **99**(14), 143116 (2011).
29. P. Krogstrup, H. I. Jørgensen, M. Heiss, O. Demichel, J. V. Holm, M. Agesen, J. Nygard, and A. F. Morral, "Single-nanowire solar cells beyond the Shockley-Queisser limit," *Nat. Photonics* **7**(4), 306–310 (2013).
30. G. Mariani, A. C. Scofield, C. Hung, and D. L. Huffaker, "GaAs nanopillar-array solar cells employing in situ surface passivation," *Nat. Commun.* **4**(1), 1497 (2013).
31. X. Li and Y. Zhan, "Enhanced external quantum efficiency in rectangular single nanowire solar cells," *Appl. Phys. Lett.* **102**(2), 021101 (2013).
32. Y. Yang, X. Peng, S. Hyatt, and D. Yu, "Broadband Quantum Efficiency Enhancement in High Index Nanowire Resonators," *Nano Lett.* **15**(5), 3541–3546 (2015).
33. G. Mariani, Z. Zhou, A. Scofield, and D. L. Huffaker, "Direct-Bandgap Epitaxial Core–Multishell Nanopillar Photovoltaics Featuring Subwavelength Optical Concentrators," *Nano Lett.* **13**(4), 1632–1637 (2013).
34. W. Liu, S. Zhang, M. L. Stutzman, and M. Poelker, "The effects of ion bombardment on bulk GaAs photocathodes with different surface-cleavage planes," *Phys. Rev. Accel. Beams* **19**(10), 103402 (2016).
35. W. E. Spicer, "Negative affinity 3–5 photocathodes: Their physics and technology," *Appl. Phys. A* **12**(2), 115–130 (1977).
36. J. Zou, B. Chang, H. Chen, and L. Liu, "Variation of quantum-yield curves for GaAs photocathodes under illumination," *J. Appl. Phys.* **101**(3), 033126 (2007).
37. FDTD Solutions, Lumerical Solutions, Inc., <http://www.lumerical.com>.
38. VisualTCAD 1.9.3, Cogenda Pte Ltd, <http://www.cogenda.com/>.
39. X. Ding, X. Ge, J. Zou, Y. Zhang, X. Peng, W. Deng, Z. Chen, W. Zhao, and B. Chang, "Photoemission characteristics of graded band-gap AlGaAs/GaAs wire photocathode," *Opt. Commun.* **367**, 149–154 (2016).
40. S. Karkare, D. Dimitrov, W. Schaff, L. Cultrera, A. Bartnik, X. Liu, E. Sawyer, T. Esposito, and I. Bazarov, "Monte Carlo charge transport and photoemission from negative electron affinity GaAs photocathodes," *J. Appl. Phys.* **113**(10), 104904 (2013).
41. C. F. Bohren and D. R. Huffman, "Absorption and Scattering by an Arbitrary Particle," in *Absorption and Scattering of Light by Small Particles*, C. F. Bohren and D. R. Huffman, eds. (John Wiley & Sons, 1998).
42. E. D. Palik, "Semiconductors," in *Handbook of Optical Constants of Solids*, vol. 1, E. D. Palik, ed. (Academic Press, 1985).
43. M. E. Levinstein and S. L. Rumyantsev, "GALLIUM ARSENIDE GaAs," in *Handbook Series on Semiconductor Parameters*, vol. 1, M. Levinstein, S. Rumyantsev, and M. Shur, eds. (World Scientific, 1996).
44. M. Sotoodeh, A. H. Khalid, and A. A. Rezazadeh, "Empirical low-field mobility model for III–V compounds applicable in device simulation codes," *J. Appl. Phys.* **87**(6), 2890–2900 (2000).
45. A. H. Trojnar, C. E. Valdivia, K. M. Azizur-Rahman, R. R. LaPierre, K. Hinzer, and J. J. Krich, "Optimization of GaAs Nanowire Solar Cell Efficiency via Optoelectronic Modeling," in *Conference Record of the 42nd IEEE Photovoltaic Specialists Conference* (IEEE, 2015), pp. 1–6.
46. T. Rahman and K. Fobelets, "Efficient tool flow for 3D photovoltaic modelling," *Comput. Phys. Commun.* **193**, 124–130 (2015).
47. X. Jin, S. Ohki, T. Ishikawa, A. Tackeuchi, and Y. Hond, "Analysis of quantum efficiency improvement in spin-polarized photocathode," *J. Appl. Phys.* **120**(16), 164501 (2016).
48. X. Jin, B. Ozdol, M. Yamamoto, A. Mano, N. Yamamoto, and Y. Takeda, "Effect of crystal quality on performance of spin-polarized photocathode," *Appl. Phys. Lett.* **105**(20), 203509 (2014).
49. J. Buencuerpo, J. M. Llorens, P. Zilio, W. Raja, J. Cunha, A. Alabastri, R. P. Zaccaria, A. Martí, and T. Versloot, "Light-trapping in photon enhanced thermionic emitters," *Opt. Express* **23**(19), A1220–A1235 (2015).